

Visualizing aerosol-particle injection for diffractive-imaging experiments

Salah Awel,^{1,2} Richard A. Kirian,^{1,3} Niko Eckerskorn,⁴ Max Wiedorn,^{1,5}
Daniel A. Horke,^{1,2} Andrei V. Rode,⁴ Jochen Küpper,^{1,2,5*} and Henry N.
Chapman^{1,2,5*}

¹Center for Free-Electron Laser Science, DESY, Notkestrasse 85, 22607 Hamburg, Germany

²The Hamburg Center for Ultrafast Imaging, University of Hamburg, Luruper Chaussee 149, 22761 Hamburg, Germany

³Department of Physics, Arizona State University, Tempe, AZ, USA

⁴Laser Physics Centre, Research School of Physics and Engineering, Australian National University, Canberra, ACT 2601, Australia

⁵Department of Physics, University of Hamburg, Luruper Chaussee 149, 22761 Hamburg, Germany

jochen.kuepper@cfel.de

henry.chapman@cfel.de

Abstract: Delivering sub-micrometer particles to an intense x-ray focus is a crucial aspect of single-particle diffractive-imaging experiments at x-ray free-electron lasers. Enabling direct visualization of sub-micrometer aerosol particle streams without interfering with the operation of the particle injector can greatly improve the overall efficiency of single-particle imaging experiments by reducing the amount of time and sample consumed during measurements. We have developed in-situ non-destructive imaging diagnostics to aid real-time particle injector optimization and x-ray/particle-beam alignment, based on laser illumination schemes and fast imaging detectors. Our diagnostics are constructed to provide a non-invasive rapid feedback on injector performance during measurements, and have been demonstrated during diffraction measurements at the FLASH free-electron laser.

© 2018 Optical Society of America

OCIS codes:

References and links

1. M. J. Bogan, S. Boutet, H. N. Chapman, S. Marchesini, A. Barty, W. H. Benner, U. Rohner, M. Frank, S. P. Hau-Riege, S. Bajt, B. Woods, M. M. Seibert, B. Iwan, N. Timneanu, J. Hajdu, and J. Schulz, "Aerosol imaging with a soft x-ray free electron laser," *Aerosol Sci. Techn.* **44**, i–vi (2010).
2. M. M. Seibert, T. Ekeberg, F. R. N. C. Maia, M. Svenda, J. Andreasson, O. Jönsson, D. Odić, B. Iwan, A. Rocker, D. Westphal, M. Hantke, D. P. Deponce, A. Barty, J. Schulz, L. Gumprecht, N. Coppola, A. Aquila, M. Liang, T. A. White, A. Martin, C. Caleman, S. Stern, C. Abergel, V. Seltzer, J.-M. Claverie, C. Bostedt, J. D. Bozek, S. Boutet, A. A. Miahnahri, M. Messerschmidt, J. Krzywinski, G. Williams, K. O. Hodgson, M. J. Bogan, C. Y. Hampton, R. G. Sierra, D. Starodub, I. Andersson, S. Bajt, M. Barthelmess, J. C. H. Spence, P. Fromme, U. Weierstall, R. Kirian, M. Hunter, R. B. Doak, S. Marchesini, S. P. Hau-Riege, M. Frank, R. L. Shoeman, L. Lomb, S. W. Epp, R. Hartmann, D. Rolles, A. Rudenko, C. Schmidt, L. Foucar, N. Kimmel, P. Holl, B. Rudek, B. Erk, A. Hömke, C. Reich, D. Pietschner, G. Weidenspointner, L. Strüder, G. Hauser, H. Gorke, J. Ullrich, I. Schlichting, S. Herrmann, G. Schaller, F. Schopper, H. Soltau, K.-U. Kühnel, R. Andritschke, C.-D. Schröter, F. Krasniqi, M. Bott, S. Schorb, D. Rupp, M. Adolph, T. Gorkhover, H. Hirsemann, G. Potdevin, H. Graafsma, B. Nilsson, H. N. Chapman, and J. Hajdu, "Single mimivirus particles intercepted and imaged with an x-ray laser," *Nature* **470**, 78 (2011).
3. R. Neutze, R. Wouts, D. van der Spoel, E. Weckert, and J. Hajdu, "Potential for biomolecular imaging with femtosecond X-ray pulses," *Nature* **406**, 752–757 (2000).

4. H. N. Chapman, "X-ray imaging beyond the limits," *Nature Mater.* **8**, 299–301 (2009).
5. D. P. DePonte, U. Weierstall, K. Schmidt, J. Warner, D. Starodub, J. C. H. Spence, and R. B. Doak, "Gas dynamic virtual nozzle for generation of microscopic droplet streams," *J. Phys. D Appl. Phys.* **41**, 195505 (2008).
6. M. J. Bogan, W. H. Benner, S. Boutet, U. Rohner, M. Frank, A. Barty, M. M. Seibert, F. Maia, S. Marchesini, S. Bajt, B. Woods, V. Riot, S. P. Hau-Riege, M. Svenda, E. Marklund, E. Spiller, J. Hajdu, and H. N. Chapman, "Single particle x-ray diffractive imaging," *Nano Letters* **8**, 310–316 (2008).
7. J. Küpper, S. Stern, L. Holmegaard, F. Filsinger, A. Rouzée, A. Rudenko, P. Johnsson, A. V. Martin, M. Adolph, A. Aquila, S. Bajt, A. Barty, C. Bostedt, J. Bozek, C. Caleman, R. Coffee, N. Coppola, T. Delmas, S. Epp, B. Erk, L. Foucar, T. Gorkhover, L. Gumprecht, A. Hartmann, R. Hartmann, G. Hauser, P. Holl, A. Hömke, N. Kimmel, F. Krasniqi, K.-U. Kühnel, J. Maurer, M. Messerschmidt, R. Moshhammer, C. Reich, B. Rudek, R. Santra, I. Schlichting, C. Schmidt, S. Schorb, J. Schulz, H. Soltau, J. C. H. Spence, D. Starodub, L. Strüder, J. Thøgersen, M. J. J. Vrakking, G. Weidenspointner, T. A. White, C. Wunderer, G. Meijer, J. Ullrich, H. Stapelfeldt, D. Rolles, and H. N. Chapman, "X-ray diffraction from isolated and strongly aligned gas-phase molecules with a free-electron laser," *Phys. Rev. Lett.* **112**, 083002 (2014).
8. P. Liu, P. J. Ziemann, D. B. Kittelson, and P. H. McMurry, "Generating particle beams of controlled dimensions and divergence: I. theory of particle motion in aerodynamic lenses and nozzle expansions," *Aerosol Sci. Technol.* **22**, 293–313 (1995).
9. R. A. Kirian, S. Awel, N. Eckerskorn, H. Fleckenstein, M. Wiedorn, L. Adriano, S. Bajt, M. Barthelmess, R. Bean, K. R. Beyerlein, L. M. G. Chavas, M. Domaracky, M. Heymann, D. A. Horke, J. Knoska, M. Metz, A. Morgan, D. Oberthuer, N. Roth, T. Sato, P. L. Xavier, O. Yefanov, A. V. Rode, J. Küpper, and H. N. Chapman, "Simple convergent-nozzle aerosol injector for single-particle diffractive imaging with x-ray free-electron lasers," *Struct. Dyn.* **2**, 041717 (2015).
10. N. Rao, J. Navascues, and J. F. De La Mora, "Aerodynamic focusing of particles in viscous jets," *J. Aerosol Sci.* **24**, 879–892 (1993).
11. W. H. Benner, M. J. Bogan, U. Rohner, S. Boutet, B. Woods, and M. Frank, "Non-destructive characterization and alignment of aerodynamically focused particle beams using single particle charge detection," *J. Aerosol. Sci.* **39**, 917–928 (2008).
12. S. Fuerstenau, A. Gomez, and J. F. de la Mora, "Visualization of aerodynamically focused subsonic aerosol jets," *J. Aerosol Sci.* **25**, 165–173 (1994).
13. G. R. Farquar, P. T. Steele, E. L. McJimpsey, C. B. Lebrilla, H. J. Tobias, E. E. Gard, M. Frank, K. Coffee, V. Riot, and D. P. Fergenson, "Supramicrometer particle shadowgraph imaging in the ionization region of a single particle aerosol mass spectrometer," *J. Aerosol. Sci.* **39**, 10–18 (2008).
14. R. J. Adrian and J. Westerweel, *Particle image velocimetry*, 30 (Cambridge University Press, 2011).
15. C. E. Willert and M. Gharib, "Digital particle image velocimetry," *Exp. Fluids* **10**, 181–193 (1991).
16. X. Wang and P. H. McMurry, "A design tool for aerodynamic lens systems," *Aerosol Sci. Technol.* **40**, 320–334 (2006).
17. S. Thoroddsen, T. Etoh, and K. Takehara, "High-speed imaging of drops and bubbles," *Annu. Rev. Fluid Mech.* **40**, 257–285 (2008).
18. M. Versluis, "High-speed imaging in fluids," *Exp. Fluids* **54**, 1–35 (2013).
19. E. Betzig, G. H. Patterson, R. Sougrat, O. W. Lindwasser, S. Olenych, J. S. Bonifacino, M. W. Davidson, J. Lippincott-Schwartz, and H. F. Hess, "Imaging intracellular fluorescent proteins at nanometer resolution," *Science* **313**, 1642–1645 (2006).
20. R. Henriques, C. Griffiths, E. Hesper Rego, and M. M. Mhlanga, "Palm and storm: Unlocking live-cell super-resolution," *Biopolymers* **95**, 322–331 (2011).
21. A. van der Bos, M.-J. van der Meulen, T. Driessen, M. van den Berg, H. Reinten, H. Wijshoff, M. Versluis, and D. Lohse, "Velocity profile inside piezoacoustic inkjet droplets in flight: comparison between experiment and numerical simulation," *Phys. Rev.* **1**, 014004 (2014).
22. R. B. Miles, W. R. Lempert, and J. N. Forkey, "Laser Rayleigh scattering," *Meas. Sci. Technol.* **12**, R33 (2001).
23. L. Li, C. Li, Z. Zhang, and E. Alexov, "On the Dielectric "Constant" of Proteins: Smooth Dielectric Function for Macromolecular Modeling and Its Implementation in DelPhi," *J. Chem. Theory Comput.* **9**, 2126–2136 (2013).
24. B. Fowler, "Single photon CMOS imaging through noise minimization," in "Single-Photon Imaging," (Springer, Berlin, Heidelberg, 2011), pp. 159–195.
25. V. Krishnaswami, C. J. F. Van Noorden, E. M. M. Manders, and R. A. Hoebe, "Towards digital photon counting cameras for single-molecule optical nanoscopy," *Opt. Nanoscopy* **3**, 1–11 (2014).
26. N. Eckerskorn, L. Li, R. A. Kirian, J. Küpper, D. P. DePonte, W. Krolikowski, W. M. Lee, H. N. Chapman, and A. V. Rode, "Hollow Bessel-like beam as an optical guide for a stream of microscopic particles," *Opt. Exp.* **21**, 30492–30499 (2013).
27. N. Eckerskorn, R. Bowman, R. A. Kirian, S. Awel, M. Wiedorn, J. Küpper, M. J. Padgett, H. N. Chapman, and A. V. Rode, "Toward steering a jet of particles into an x-ray beam with optically induced forces," in "SPIE Optics + Photonics," (SPIE, San Diego, California, United States, 2015), p. 9548–18.
28. N. Eckerskorn, R. Bowman, R. A. Kirian, S. Awel, M. Wiedorn, J. Küpper, M. J. Padgett, H. N. Chapman, and A. V. Rode, "Evaluation of optically induced forces imposed in an optical funnel on a stream of particles in air and

- in vacuum,” *Phys. Rev. Appl.* **4**, 064001 (2015).
29. C. Willert and M. Gharib, “Three-dimensional particle imaging with a single camera,” *Exp. Fluids* **12**, 353–358 (1992).
30. J.A. Guerrero-Viramontes, D. Moreno-Hernandez, F. Mendoza-Santoyo, and M. Funes-Gallanzi, “3D particle positioning from CCD images using the generalized Lorenz-Mie and Huygens-Fresnel theories,” *Meas. Sci. Technol.* **17**, 2328–2334 (2006).
31. N. Vervoort, D. Daemen, and G. Török, “Performance evaluation of evaporative light scattering detection and charged aerosol detection in reversed phase liquid chromatography,” *J. Chromatogr. A* **1189**, 92–100 (2008).
-

1. Introduction

The emergence of x-ray free-electron lasers (XFELs) has inspired the development of new particle-injection instruments capable of delivering nano- and micro-particles to the intense 0.1–5 μm focus of a few-femtosecond duration x-ray beam. Single-particle diffractive imaging (SPI) is among the methods that rely on the development of such particle-beam injectors, as it requires a series of isolated molecules, viruses, cells or microcrystals to be directed across the x-ray beam. Three-dimensional diffraction intensity maps can be constructed by assembling numerous two-dimensional diffraction patterns from particles exposed in different orientations [1, 2]. In this way, three-dimensional images can be formed from reproducible targets. If successful, SPI will allow for the determination of high-resolution structures of radiation-sensitive targets [3], without the need to grow large well-ordered crystals, which is often the principal bottleneck to macromolecular structure determination.

In SPI experiments, it is important to precisely deliver the target particles to the most intense region of the focused x-ray beam in rapid succession, since each particle is completely destroyed through photoionization-induced damage processes [4]. Liquid jets formed by gas-dynamic virtual nozzles (GDVN) [5], aerodynamic aerosol focusing [6], or gas-phase supersonic jet/molecular beam injectors [7] are among the most common techniques used to deliver particles. For SPI work, gas-phase injectors are preferred since a surrounding liquid reduces contrast and increases background scatter, which makes data analysis difficult, if not impossible. Aerodynamical-lens-stack aerosol particle injectors (ALS) [8] are presently the most common injector used for SPI experiments, which can create a collimated aerosol beam when particles suspended in a carrier gas pass through a series of concentric apertures. Alternative injectors, e. g., convergent-orifice nozzles, are also under development for SPI experiments [9].

During SPI experiments, aerosol injectors must be monitored frequently in order to maintain optimal hit fraction and delivery efficiency, i. e., the fraction of x-ray pulses that intercept a particle and the fraction of particles that are intercepted by an x-ray pulse, respectively. Particle-beam diagnostics are important because XFEL facilities are costly to operate, and many samples are also costly to obtain in significant quantities. X-ray diffraction patterns themselves are the ultimate diagnostic of injection efficiency, but this diagnosis is limited by the XFEL pulse repetition rate, detector readout rate, data processing rate, and availability of the x-ray source. It is desirable to have complimentary real-time diagnostics that assist the injection optimization process, both offline as well as online, during diffraction measurements. As we show below, direct visualization of particle beams through laser illumination is a simple yet powerful means to optimize injection efficiency. In addition to improving SPI experiment efficiency, imaging diagnostics can greatly accelerate the development of new aerosol injector schemes.

Aerosolized nanoparticles are not easily visible, and particle injection environments are not always easily accessible for probing due to ancillary measurement tools. Therefore, *in-situ* diagnostics can be challenging to implement within existing x-ray diffraction apparatuses. Early experimental work utilized greased plates onto which aerosol particles adhere [10, 11], allowing the transverse particle beam profile to be estimated. This method is commonly employed in SPI experiments, however such particle depositions, examined under a microscope, are not

easy to interpret quantitatively. In the context of SPI work, the first detailed experimental characterization of aerodynamically focused particles was carried out by Benner et al. [11]. Here, particle velocities and positions were determined from the image charges of particles transmitted through a metal tube. Aerosol beams have also been directly imaged in the past [12, 13], but so far the great utility of this approach that we emphasize here has not been integrated into SPI experiments. More generally, the determination of particle-laden flow fields has been studied extensively within the field of particle image velocimetry (PIV) and its variants [14, 15].

In this paper, we present simple direct optical imaging diagnostics for online monitoring of particle injection during XFEL experiments, as well as for general aerosol beam characterization and injector optimization. We have utilized both continuous-wave (CW) and pulsed nanosecond illumination along with high-speed cameras, and nearly real-time analysis software, that can measure particle speeds, injector transmission efficiency, and projected particle beam density profiles. We have also implemented an in-vacuum inverted microscope for imaging particles that adhere to a gel.

2. Theory and Background

2.1. Efficiencies of single-particle imaging

Direct optical imaging can reveal most of the key parameters needed to optimize SPI sample injection, which we discuss here. The first key parameter is known as the “hit fraction” or “hit rate”, and is equal to the fraction of x-ray pulses that intercept a particle. For femtosecond XFEL illumination, this quantity depends on the instantaneous projection of the particle number density along the x-ray beam path, and can be approximated as $H \approx fT\sigma/(vd)$, where f is the rate at which particles enter the injector, T the injector transmission efficiency (ratio of the number of particles that enter and exit the injector), σ the effective illumination area that produces useful diffraction, v the velocity of the particles, and d the particle beam diameter. In this formulation, we assume that the particle beam has a diameter smaller than the depth of focus of the x-ray beam, which is almost always satisfied in SPI experiments. We also assume that the x-ray beam diameter is significantly smaller than the particle beam diameter. We assume that $H < 1$, since x-ray diffraction patterns containing multiple particles illuminated simultaneously tend to complicate the diffraction analysis.

Another key parameter is known as the “delivery efficiency”, equal to the fraction of consumed particles that are intercepted by an x-ray pulse. Delivery efficiency for continuous flow of particles can be approximated as $\varepsilon \approx HF/f$, where F is the XFEL pulse repetition rate, and it is assumed that $F \ll f$. Notably, a hit fraction of $H \approx 1$ can be achieved while having delivery efficiency $\varepsilon \ll 1$.

In order to score a higher hit fraction and delivery efficiency, one typically needs to find an optimal compromise between the three parameters v , d , and T . Importantly, for a given injector geometry, it might not be possible to vary these parameters independently of each other [16]. Different types of injectors can also introduce tradeoffs – for instance, a convergent-orifice injector can create a tightly focused particle beam that approaches the size of micro-focused x-ray beams, but apparently produces particles with greater speeds than typical ALS injectors [9]. Tightly focused beams *necessitate* the use of an *in-situ* direct imaging system since one would otherwise need to perform a three-dimensional scan of the x-ray beam in order to properly position the interaction region, whereas a collimated particle beam requires only a two-dimensional scan.

In general, independent of the type of injector used, the aerosol beams we consider here are composed of fast, nearly-unidirectional, and sparsely placed small particles confined to a narrow beam in a low-pressure environment. Typically, on the order of 10^7 particles enter the injector per second and expand into the vacuum with a speed that can reach several hundred

m/s. This leads to hit fractions well below 0.1% for current injectors and nano-focused x-ray beams, thus rendering x-ray diffraction-based diagnostics inefficient, highlighting the need for complementary rapid-feedback diagnostics.

2.2. Direct side-view particle imaging schemes

We can classify the direct side-view imaging of particles presented here into three regimes, principally identified by three characteristic times: $\tau = d/v$ – the time it takes for a particle with velocity v to move over its diameter d , exposure time t_{exp} – the camera integration time or duration of the illumination pulse, and t_{fov} – the time taken for a particle to move across the full field of view (FOV). d is the diffraction-limited spot size of the particle if the particle is smaller than the resolution limit of the of the imaging system.

2.2.1. “Long exposure” imaging

In the “long exposure” mode, the particle beam is illuminated either with a continuous or pulsed light source with a very long exposure time ($t_{\text{exp}} \gg t_{\text{fov}}$) on the camera [12]. This mode does not allow for the determination of particle velocities, but is straightforward to implement with relatively inexpensive equipment. In many cases the resulting integrated image intensity is directly proportional to the projection of the particle density along the optical axis. However, since elastic scattering in both the Mie and Rayleigh regime scales exponentially with particle diameter (for Rayleigh scattering, the intensity scales with the sixth power of particle diameter), one must ensure that all particles are of the species of interest, and not aggregated clusters of particles (for example) that would tend to dominate the intensity profile of the image.

2.2.2. “Streak” imaging

Visualizing *individual*, fast-moving, sub-micrometer particles requires $t_{\text{exp}} < t_{\text{fov}}$, such that the entire image is contained within the field of view. In the “streak” imaging mode, t_{exp} is chosen such that particles appear as streaks across the imaging plane ($\tau < t_{\text{exp}} < t_{\text{fov}}$). If t_{exp} is known and the entire streak is contained in the image, the velocity can be determined from the streak length. If the particle density is sufficiently low to avoid overlapped particle images, the number density of particles can also be determined by analyzing the intensity centroid of each streak. Ideally, the illumination source should have a well-defined top-hat temporal profile as well as uniform spatial intensity profile. This can be achieved with CW lasers, provided a fast shutter is available for either the laser or the imaging device. Longer streak lengths lead to better measurement accuracy, but also increase the chance of particle streaks overlapping and of streaks that partly fall out of the field of view. The optimum t_{exp} should be chosen according to these two factors.

2.2.3. “Snapshot” imaging

In the “snapshot” imaging mode, when $t_{\text{exp}} \ll \tau$, point-like particle images are produced on the detector, mitigating motion blur [17, 18]. For example, particles moving at $v = 200$ m/s with $d = 1$ μm require a 5 ns exposure time to freeze the motion. The snapshot image can be achieved with short camera integration times or short illumination sources, e. g., pulsed lasers, flash lamps, or spark discharges [14]. We note that in the cases of streaked and snapshot imaging modes, one can determine particle positions at a resolution better than the resolution of the optical system through intensity centroid analysis, akin to super resolution microscopy molecule localization techniques [19, 20]. The snapshot imaging mode has several advantages over the long-exposure imaging mode: it enables straightforward quantitative determination of particle beam density, and in principle one can infer particle volumes through integrated scattering intensity, if the system is well calibrated. The velocity and acceleration of particles can also be measured from

snapshot images with the use of multiple exposures with known delays, provided that all particle images appear in the same field of view [14, 21].

Provided that detector readout noise is not significant, snapshot imaging maximizes the signal-to-noise ratio (SNR) since unnecessary exposure time is avoided, and all scattered light entering the optics is focused to a single resolution element. Imaging based on continuous illumination and short camera integration time usually suffers from lower signal levels compared with pulsed illumination (assuming similar average optical power). This is due to the fact that in the latter case the intensity of a particle image is fixed by the intensity of the illumination, whereas in the former case only a small fraction of the CW laser power is used to illuminate the particle, i. e., most of the laser power is unused [14, 17].

2.3. Transverse-plane particle imaging

Simple imaging of the transverse profile of the particle beam can be achieved with the help of a flat, sticky surface placed transverse to the particle beam propagation. The particle beam diameter can be roughly estimated from the deposition of particles on the plate, imaged either directly *in-situ*, or by analyzing the deposition under an external microscope [10, 11]. Unlike side-view imaging techniques, this does not contain any information regarding particle dynamics, but nonetheless gives useful and rapid feedback on the performance of an injector. For instance, asymmetry of the particle beam in the transverse plane is difficult to observe with side-view imaging, but can be observed easily using this technique.

2.4. Laser scattering intensity

Imaging sub-micrometer particles through elastic scattering raises considerable concerns regarding scattering intensity at the detector. As we show below, a relatively modest setup can be used to image particles with diameters of a few hundred nanometers, where Mie scattering dominates. Mie scattering theory is typically applied for particle diameters down to approximately one tenth of the scattering wavelength, below which the simple Rayleigh theory becomes applicable. The latter is generally considered valid for the case $d\pi/\lambda < 1$, where d is the particle diameter and λ the wavelength of light. For a wavelength of 532 nm, this corresponds to $d \sim 170$ nm. In the regime $\sim 50 - 170$ nm both Mie and Rayleigh theories can be considered valid and yield comparable scattering cross-sections (see below). However, they differ significantly in theoretical treatment. Mie theory is based on an infinite series of spherical partial waves to describe scattering, whereas the Rayleigh approximation can be summarized as a single analytical expression. The former calculates the (complex) scattering phase functions, and therefore yields a directional scattering dependence, while Rayleigh theory assumes an isotropic scattering distribution (apart from a polarization correction). In the following basic theoretical treatment we focus on Rayleigh scattering theory, due to its mathematical simplicity and because it is a valid approximation in the size range of typical biological molecules.

The total Rayleigh scattering cross section for a sphere of diameter D and relative permittivity ϵ is [22]

$$\sigma = \frac{8\pi^5 d^6}{3\lambda^4} \left(\frac{\epsilon - 1}{\epsilon + 2} \right)^2 \quad (1)$$

For a beam of diameter g and pulse energy E_0 , the scattered energy is $E = 4E_0\sigma/\pi g^2$, and the number of scattered photons is $N = E\lambda/hc$, where h is Planck's constant, and c is the speed of light. Thus, we have

$$N = \frac{32E_0\pi^4 d^6}{3\lambda^3 g^2 hc} \left(\frac{\epsilon - 1}{\epsilon + 2} \right)^2 \quad (2)$$

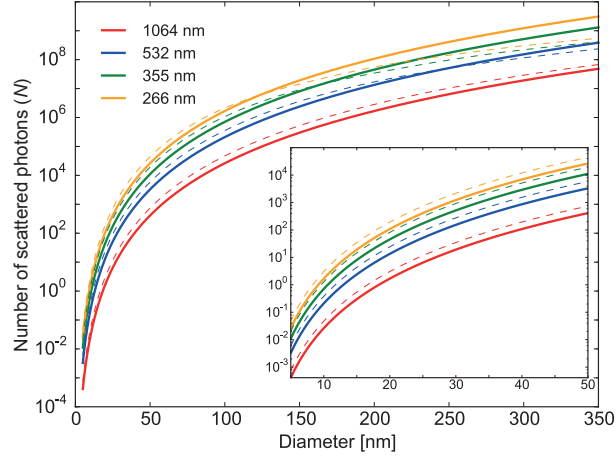


Fig. 1. Total number of scattered photons as a function of particle diameter for several wavelengths. Solid lines are calculated using the Rayleigh formalism, dashed lines are calculated from Mie theory. The calculation is done for 100 mJ pulses ($N_0 \approx 10^{17}$ photons) focused to a top-hat spatial intensity profile with diameter $\omega_0 = 1$ mm.

The relative permittivity for proteins can vary significantly [23], but $\epsilon \approx 2-4$ is a reasonable assumption; polystyrene has $\epsilon \approx 2.6$. Fig. 1 shows total scattering calculations for the Rayleigh and Mie regime for different particle diameters and laser wavelengths for the case $\epsilon = 2.6$. We must reduce the total scattered photon number N according to the fraction of photons observed. This results in a number of photons N_Ω captured in the solid angle Ω of the optical system. Neglecting polarization factors, we obtain

$$N_\Omega = \frac{16E_0\pi^4d^6}{3\lambda^3g^2hc} \left(\frac{\epsilon - 1}{\epsilon + 2} \right)^2 (1 - \cos\theta) \quad (3)$$

where θ (measured from the optical axis of the imaging system) is the maximum scattering angle collected by the optical system (the numerical aperture is defined as $\text{NA} = \sin\theta$). This provides a lower bound for experiments with the polarization axis of a linearly-polarized laser perpendicular to the optical axis of the imaging system.

The SNR of an imaging system depends on several factors. Since the typical size of single particle scattered intensity spans very few pixels on the detector, a pixel will collect approximately N_Ω photons from a particle. If the dominant noise sources of the imaging chip are the dark current, readout noise, background photons, and Poisson noise, the signal-to-noise ratio can be expressed as

$$\text{SNR} = \frac{N_\Omega Q}{\sqrt{N_\Omega Q + N_b Q + N_d + \sigma_r^2}} \quad (4)$$

where Q is the quantum efficiency of the chip (number of electrons per photon), N_d is the mean number of dark current electrons, σ_r is the RMS readout noise (in number of electrons), and N_b is the number of background photons per pixel. This estimate assumes that all photons collected by the objective are directed to a single pixel. As an example, the camera utilized in our measurements (Photron SA4) contains a CMOS chip that has a readout noise of 38 electrons, and a quantum efficiency of about 33% at 530 nm. Assuming that background photon levels can be reduced to nearly zero, a minimum of about $38/0.33 \approx 120$ photons per pixel would be required to obtain a SNR of 1 with this chip. Factoring in the collection angle of the optics, we can roughly estimate that particles down to about 50 nm could likely be imaged with this

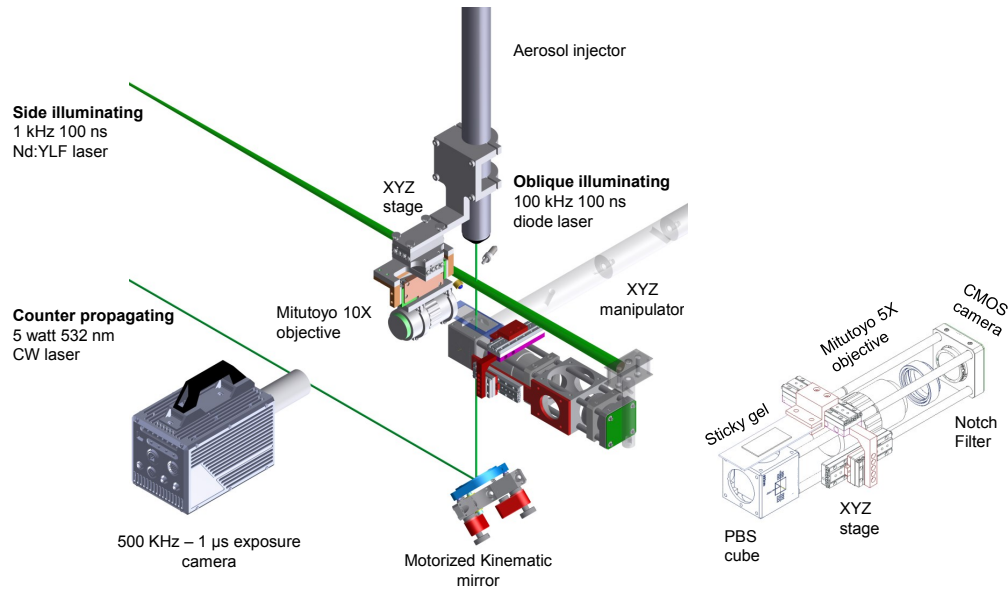


Fig. 2. A schematic diagram of the basic direct aerosol imaging set-up. The in-vacuum microscope assembly is shown to the right.

detector. Smaller particles may require the use of single-photon detectors, such as EMCCD and SPAD detectors [24, 25].

3. Experimental setup

Our experiment is constructed within a vacuum chamber that hosts an aerosol injector and, in some cases, x-ray diffraction detectors. For nebulization we use a gas-dynamic virtual nozzle (GDVN) [2, 5]. The aerosol stream is delivered either by an ALS injector (Uppsala University, Sweden) or by a convergent-nozzle injector [9].

Side-view imaging in all three modes is implemented using a high-speed imaging configuration based on a high-frame-rate camera or on pulsed-illumination, as shown in Fig. 2. Imaging in the transverse plane is achieved with an inverted in-vacuum microscope that views particles as they adhere to a glass microscope slide coated with a sticky purified gel film (TELTEC, P/N DGL-20/17-X8).

3.1. Side-view imaging configuration

The key components in our side-imaging system are a high-frame-rate camera, both pulsed and CW illumination lasers, and imaging optics optimized for either a wide field of view or a high magnification. We discuss these components and their configurations below. We generally work in a quasi-dark-field imaging mode, where images are formed from scattered light without allowing the direct beam to enter the optical system. For wide-field views, we use a long-working-distance (LWD) microscope (Infinity model K2, working distance 225–300 mm, depth of focus (DOF) $\approx 100 \mu\text{m}$, magnification 2.13, and FOV $11.7 \times 11.7 \text{ mm}^2$) mounted outside of the vacuum chamber. For high-magnification views, a $10\times$ infinity-corrected objective (Mitutoyo, working distance 38 mm, DOF $3.5 \mu\text{m}$, magnification 28, FOV $850 \times 850 \mu\text{m}^2$) is used, mounted on a three-axis motorized stage inside the vacuum chamber. Switching between these two configurations only involves swapping in/out the K2 objective and translating the

high-magnification objective into position. The scattered light from the particle beam exits the chamber through a standard viewport and forms an image on a translatable high-frame-rate CMOS camera (Photron SA4) that is typically located about 350 mm outside of the chamber, see Fig. 2.

Our illumination system consists of three different optical lasers and two different illumination geometries. In the first configuration the full particle beam is illuminated with a collimated, counter-propagating CW laser (Coherent Verdi V5, 532 nm, 5 W), as depicted in Fig. 2. The laser beam is expanded and collimated not only to illuminate the whole particle beam, but also to avoid particle deflection [26–28] and damage from the tightly focused beam. This geometry allows one to introduce a second illumination source or two simultaneous viewing axes and an x-ray beam for diffractive imaging. The latter has been implemented during SPI experiments at the FLASH FEL facility in Hamburg, as discussed in subsection 4.4. In the second illumination configuration we use a laser beam propagating perpendicular to the particle beam direction, as shown in Fig. 2. This can be implemented alongside a counter-propagating illumination scheme. We have utilized two short-pulse lasers, either a Nd:YLF laser (Spectra Physics Empower ICSHG-30, 527 nm, pulse duration 100 ns, repetition rate 1 kHz, pulse energy 20 mJ, average power 20 W), or a fiber-coupled diode laser (DILAS High-Power Diode Laser IS21.16-LC, 640 nm, average power 10 W). The latter is powered by high speed diode driver (Dr. Heller Elektronik, UHS-500-12.8 A, repetition rate up to 1 MHz, pulse durations 10–100 ns) and mounted in oblique orientation to maximize forward scattering. The diode laser is the least expensive option and delivers a top-hat intensity profile.

3.2. *Transverse-plane imaging configuration*

An inverted microscope is located directly below the aerosol injector to image 2D transverse beam profiles in real time, as shown in Fig. 2. A $5\times$ infinity-corrected objective forms images as particles adhere to a transparent gel on a microscope slide that is manipulated with a three-axis translation stage. A polarizing beam splitter is mounted below the microscope slide, which allows scattered light to be imaged while the counter-propagating laser illuminates the particle beam for side-view imaging. The entire microscope assembly is mounted on a three-axis motorized stage so that it can be moved in and out of the interaction region during experiments, or translated along the axis of the injector to probe the particle beam at variable distances from the tip of the injector. In addition to producing transverse views of the particle beam, the microscope slide is used to protect the counter-propagating laser optics (since few particles adhere to the bare glass slide) as well as to align the laser beam to the particle beam. This alignment is done by iteratively tilting the laser beam or translating the injector while viewing the particle/laser overlap at two different distances (50 mm apart) along the axis of the injector.

4. Experimental results and discussion

4.1. *Side-view imaging*

Representative images from our side-view imaging scheme are shown in Fig. 3 for the different imaging modes introduced in subsection 2.2. Fig. 3(a), 3(b), and 3(d) show images of $d = 2\ \mu\text{m}$ polystyrene-sphere particles (PS), and in Fig. 3(c) shows an image of $d \approx 300\ \text{nm}$ GV particles. The PS particles were injected with an ALS, whereas GV particles were injected with a convergent-nozzle injector. Fig. 3(a) shows a typical long-exposure image collected with counter-propagating CW beam illumination, which may be interpreted as a projection of the particle beam density since the particle size distribution is relatively narrow ($< 5\%$). The results of streak beam imaging for particles moving at two different speeds are shown in Fig. 3(b) and 3(c). Fig. 3(b) shows particle streaks recorded using counter-propagating CW beam illumination and a short integration time of $13.5\ \mu\text{s}$ on the camera, while Fig. 3(c) is recorded with illumination

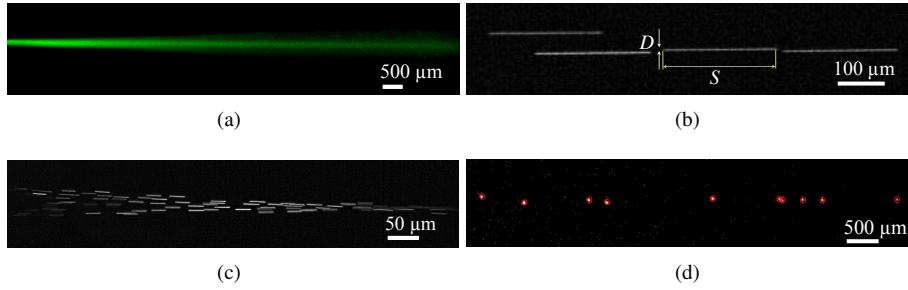


Fig. 3. Experimental particle-beam images. (a) Long-exposure image with CW laser illumination and 2 s camera exposure. (b) Particle-streak image of 2 μm PS moving at 18 m/s using CW laser illumination and a 13.5 μs camera exposure time. The length S and width D of the particle streak are marked in the image. (c) Streak image of Granulovirus (GV) particles size 200 nm \times 200 nm \times 400 nm moving at a speed of 240 m/s, using 100 ns diode laser illumination and a 1 ms camera exposure time (100 pulses in the single camera exposure). (d) Snapshot image of 2 μm PS particles using 100 ns pulses from the Nd:YLF laser and 20 ms camera exposure (20 pulses in the single camera exposure). The center of the red circle depicts centroid of a particle snapshot.

by multiple 100-ns laser pulses and a long camera integration time of 1 ms. A snapshot image with $t_{\text{exp}} < \tau$ of 2 μm PS moving at approximately 18 m/s is shown in Fig. 3(d). Here, short illumination times (100 ns) and relatively slow particle speed lead to distinct single spots on the camera, highlighted in Fig. 3(d) by red circles, which are centered around the calculated centroid positions of individual particles.

In the following we demonstrate how these data can be used to reconstruct the particle-beam density and velocity distributions. Two-dimensional particle density maps generated from raw side-view images are shown in Fig. 4. For CW illumination in the long-exposure mode, the image intensity is directly proportional to the projected particle density, provided that only a single particle species is present. This allows for direct monitoring of the injector behavior through the observation of relative image intensities, but does not readily allow for a quantitative evaluation of particle number densities without careful calibration measurements. On the other hand, streak and snapshot imaging modes allow for direct and quantitative measurements of the particle beam density without the need for intensity calibrations, since particle image centroids (for both streaks or spots) can be determined with a precision better than diffraction limit [19, 20]. From these centroids (seen in Fig. 3(d)), projected particle density maps can be produced, which allow quantitative estimates of expected hit fractions in SPI experiments.

The streak imaging technique allows for the estimation of particle velocities through evaluation of the streak length with a single pulse using a well-calibrated imaging system, as indicated in 3(b). A velocity measurement is also feasible using snapshot imaging if more than one illumination pulse occurs while the particle is in the field of view, either in the same frame or successive frames. We note several pitfalls that need to be avoided for accurate determination of particle velocity distributions from side-view imaging measurements:

1. The temporal illumination intensity profile of a pulsed laser source will be reflected in the spatial intensity of the particle streak; often one might observe long, faint trails from each particle, due to a slow decay of the laser pulse intensity. An accurate determination of the velocity requires knowledge of the temporal laser profile to disentangle the spatial image of the particle. Ideally, the illumination source should have a top-hat temporal profile.
2. Particles moving out of the illuminated volume or FOV during the exposure time will

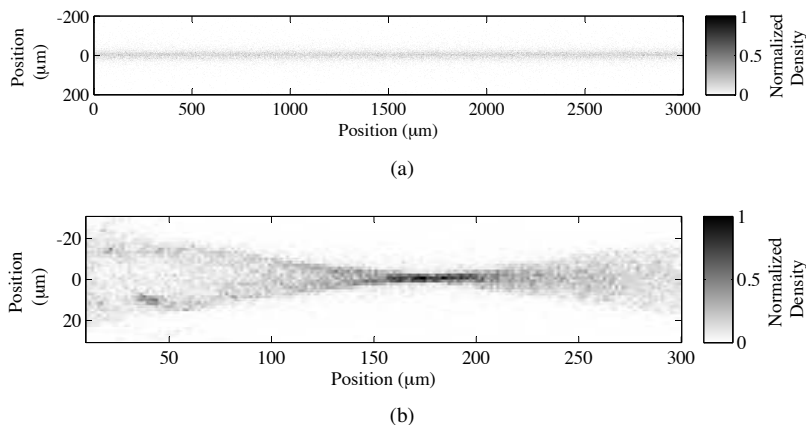


Fig. 4. The 2D projected particle density map of (a) 2 μm PS focused by the ALS and (b) 500 nm PS focused with the converging capillary injector.

appear to produce shorter streaks. This can be avoided by ensuring the illumination to be large enough to cover the entire particle beam in the FOV and ignoring streaks that lead to the edge of the image during velocity analysis.

3. Particles that move outside of the depth-of-focus of the imaging system will result in de-focused images and in some cases non-uniform streaks. If not corrected for, this will result in systematic errors in velocity estimates. However, the inclusion of image de-focus in the analysis algorithm could, in principle, reveal 3D information from a single view upon careful calibration [29, 30]. For the narrow particle beams considered here, de-focus is typically not a significant problem and can be ignored.

Once particle densities and velocity distributions are obtained, the injector transmission efficiency can be determined by comparing the rate (R_{in}) at which particles enter and the rate (R_{out}) at which they leave the injector. R_{out} can be calculated from the expression $n = R_{\text{out}}l/v$, where n is the total number of particles contained within a planar slab of thickness l , where particles are injected at a frequency f at a velocity v in the direction normal to the slab [9].

4.2. Transverse-plane imaging

Poorly performing injectors sometimes generate asymmetric particle beams, analogous to astigmatism in optical systems. This is not readily detectable in side-view imaging configurations, but is clearly visible through transverse-plane imaging with the inverted microscope discussed previously. Fig. 5 shows particle-deposition images at different distances from the tip of an ALS injector, and a clear variation in particle beam asymmetry with position. For particles larger than 1 μm , individual particles can be detected as they adhere to the gel, allowing semi-quantitative analysis of the particle beam width on the transverse plane in real time, as shown in Fig. 5 (c). However, the accuracy of the analysis is limited by our understanding of how particles adhere to the gel surface – most importantly, how the likelihood of particle adherence changes with time, e. g., as particles accumulate. For particles on the order of 100 nm or smaller, a detectable particle-deposition image is obtained after a few seconds of accumulation time, depending on the concentration and size of particles.

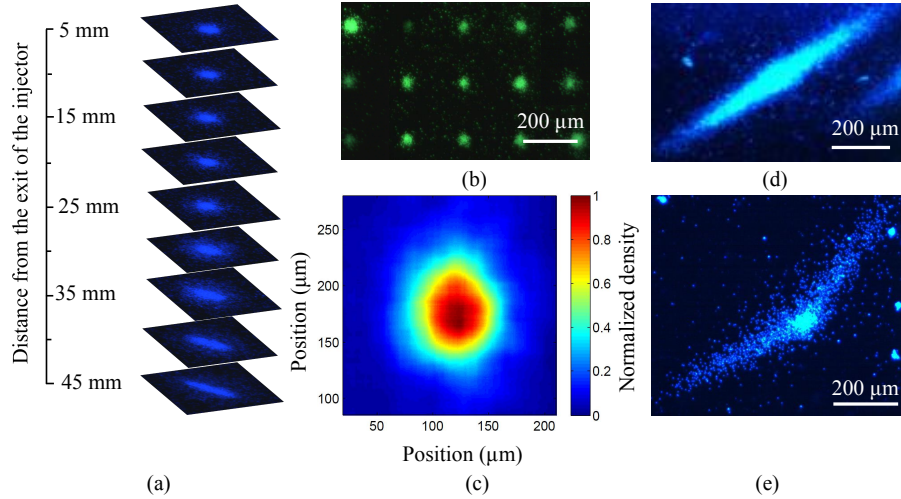


Fig. 5. Imaging of 2 μm PS particles from a beam focused by an ALS injector and deposition on transparent gel through an in-vacuum inverted microscope. (a) A series of images recorded at different distances from the injector tip. (b) A lateral scan of the microscope slide at a distance of 35 mm from the injector tip, recording particle distributions following a 1 min particle deposition per spot. (c) The transverse particle-beam density profile obtained in a measurement similar to (b), but under conditions where individual particles could be observed and their centroids determined. (d, e) 1 min particle depositions from a poorly performing injector, which, perhaps, is caused by dispersion in particle sizes and/or asymmetry in the particle source at the inlet of the injector.

4.3. Injector optimization

The presented characterization methods offer a powerful means to optimize the performance of particle injectors, both *online* during SPI measurements at XFEL facilities, as well as offline in the preparation laboratory. As discussed in section 2, the 2D projected number density of the particle beam is the most important parameter that needs to be optimized, since it scales directly with the hit fraction in an SPI experiment. The hit fraction depends on particle velocity, injector transmission, and particle beam diameter, which are ideally measured independently while developing and optimizing aerosol injectors. Fig. 6(a) shows a typical plot for injector optimization, including the velocity and particle-beam diameter in the case of 2- μm PS particles measured 35 mm downstream from the tip of the injector, as a function of the upstream pressure of the injector. The downstream chamber pressure is maintained below 10^{-2} mbar and does not significantly effect the particle speed or beam diameter. The velocity increases linearly with the upstream pressure. However, the particle beam size exhibits a distinctive minimum around 30 μm FWHM, at an upstream pressure of 0.63 mbar. As seen from Fig. 6(b), the particles are moving at an average velocity of 18.49 m/s with standard deviation of 0.28 m/s at this upstream pressure. Ignoring the transmission efficiency for now, the optimum operating pressure of the injector for maximum hit fraction should be chosen such that the product of these two parameters is minimized (see section 2), i. e., for 2 μm PS particles, the injector should be operated at 0.6 mbar for maximum hit fraction. Alternatively, one may simply measure the projected particle beam density, which automatically accounts for the contributions of velocity, transmission efficiency, and particle beam diameter. In practice, the assumption of a constant transmission efficiency is not valid over a large pressure range, and this needs to be taken into account. We note that using streak or multiple-exposure snapshot imaging allows a quantitative measure of the transmission

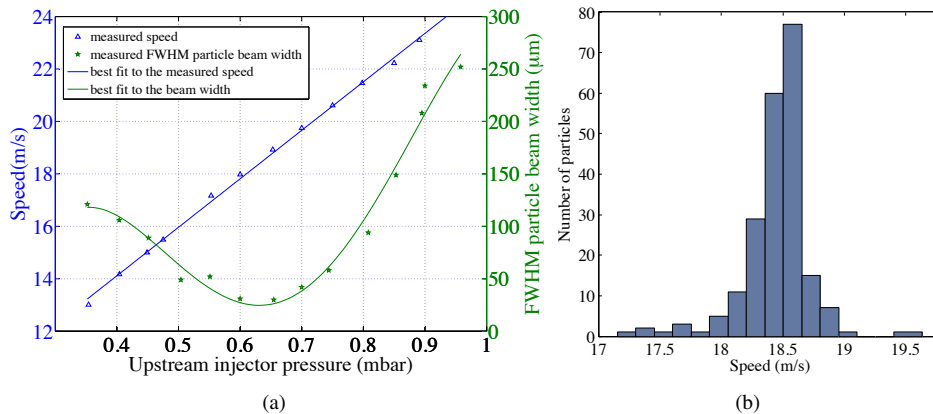


Fig. 6. Injector-performance measurement for 2 μm PS particles focused by the aerodynamic-lens-stack aerosol injector. (a) Particle velocities and projected density *versus* injector upstream pressure. (b) Velocity distribution of the particles at 0.65 mbar upstream pressure.

efficiency.

4.4. Integration with x-ray experiments

We demonstrated the utility of optical particle-beam imaging using a custom SPI experimental apparatus at the FLASH free-electron laser facility in Hamburg, Germany. Due to space limitations, we utilized a counter-propagating 5W CW laser, as shown in Fig. 7. An in-line microscope with a long-exposure CCD was placed on the same axis as the x-rays, in addition to a high-speed camera that imaged the particle beam from a viewpoint perpendicular to the x-ray beam axis. This enabled us to have, simultaneously, two orthogonal side views of the particle beam. The long exposure images from the in-line microscope were used to position of the injector for maximum hit rate, whereas images from the high-speed camera were used to position the beam with respect to the x-ray focus and to provide real-time estimates of the particle velocity and number density. As seen from subsection 3.1, the counter-propagating illumination scheme leaves plenty of spaces around the interaction region for multiple views and additional diagnostics. However, it requires careful alignment of the laser with the particle beam, especially for the case of CW lasers that must be focused to smaller diameters (approximately 100 μm in this particular case) than pulsed lasers of equivalent average power. We therefore installed translation and tilting stages inside the vacuum chamber for steering and translating the laser beam. In order to mask the scattering light from the injector tip we constructed a light shielding around the objective lens. As seen in Fig. 7, once the CW laser is properly aligned, the average intensity from a beam of GV particles is easily visible to a typical CCD (in this case, a consumer single-lens reflex camera). The ability to immediately see a particle beam drastically reduced the time needed to align the injector, and immediately revealed the typical fluctuations in the injector transmission efficiency.

5. Summary and conclusion

We demonstrated the utility of direct optical imaging of micro- and nano-particle aerosol beams for the purpose of improving the overall efficiency of single-particle x-ray diffractive imaging (SPI) experiments. We find that direct imaging of the particle beam is a straightforward means to quantitatively measure particle density maps, particle velocity distribution, and injector

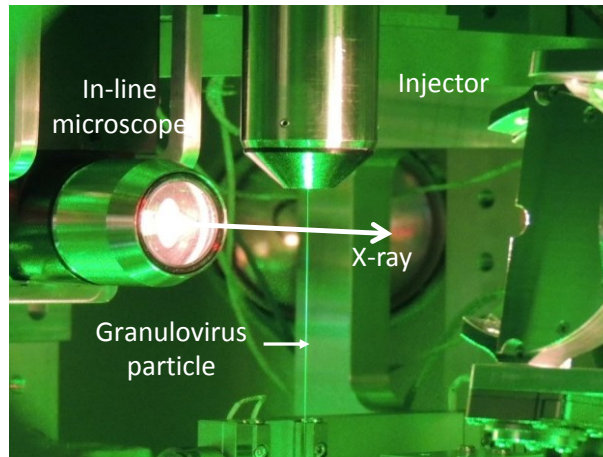


Fig. 7. The SPI setup at FLASH. The photograph of the setup shows the space around the interaction region of the laser beam with a stream of GV. This photo was taken by a DSLR camera through a window on the experimental vacuum chamber.

transmission efficiency, which are key diagnostics for optimizing SPI experiments at large-scale x-ray facilities where the time available for measurements is rather limited. A modest setup with an off-the-shelf CW laser of $\sim 1\text{--}5$ W power can readily reveal the time-averaged position and width of a typical particle beam, which greatly simplifies the procedure of positioning the injector with respect to the x-ray beam. The overall brightness of the particle beam is also indicative of the injector performance. Remarkably, such a simple diagnostic can save many hours of effort, and corresponding facility costs, compared to “shooting blind”, i. e., when injection is optimized based on x-ray diffraction data. We also showed that pulses of well-defined duration as well as a CW laser combined with a camera with a fast shutter can simultaneously produce quantitative particle-density and velocity-distribution maps. Our side-view imaging schemes were complemented by a compact in-vacuum microscope that enables indirect particle beam imaging in the transverse plane, which readily reveals particle-beam astigmatism that is not easily observed from viewpoints that are orthogonal to the particle beam.

In the configurations considered here, we have also imaged individual 200 nm diameter particles moving at speeds of 300 m/s [9] with a modest short-pulse laser (100 ns and 10 W average power). Simple scattering estimates suggest that much smaller particles, perhaps down to few tens of nanometers, should also be visible with a sufficiently intense illumination (approximately 100 mJ pulses focused to about 1 mm diameter) and a very-high-sensitivity imaging device. Although velocity measurements can be made from short pulses that create streaked particle images, it appears that the optimal method for determining velocities, from a signal-to-noise standpoint, is through the use of two time-delayed pulses of duration short enough to produce “snapshot” diffraction-limited particle images. Pulse durations of approximately 5 ns are required to freeze the motion of particles moving at 200 m/s for an image resolution of $1\ \mu\text{m}$, but Q-switched lasers that produce such pulses are common and relatively inexpensive.

We tested three different imaging modes that differ in terms of illumination geometry, optics, and the illumination source. Each of them can be implemented relatively straightforwardly in typical SPI experiments with only minor modifications. A counter-propagating geometry, in which the particle and laser beams oppose each other, maximizes the space available for ancillary diagnostics such as time-of-flight spectrometers, but requires a transparent shield to maintain clean beam-steering optics below the injector and unnecessarily exposes upstream particles to

laser illumination. For imaging the smallest of particles, it may become necessary to operate above the damage threshold of the particles. Hence, a transverse illumination scheme would be required to avoid damaging particles prior to probing with x-rays.

Thus far, our apparatus has been used to characterize the injection process downstream of the injector, close to the interaction region of particles and x-rays. It would be advantageous to include similar imaging diagnostics at positions upstream of the injector exit, so that the aerosol formation and pre-collimation (prior to focussing) can also be monitored and de-coupled from the downstream particle-beam focusing components. Ideally, these diagnostics would be extended to include particle size measurements through careful calibrations of integrated scattering intensity, Mie scattering profiles, or other interferometric methods. Such *in-situ* measurements would allow us to monitor particle aggregation and evaporation rate of the liquid buffer from the initial droplets generated by the nebulization device [31].

Acknowledgments

In addition to DESY, this work has been supported by the excellence cluster “The Hamburg Center for Ultrafast Imaging—Structure, Dynamics and Control of Matter at the Atomic Scale” of the Deutsche Forschungsgemeinschaft (CUI, DFG-EXC1074) and by the Australian Research Council’s Discovery Projects funding scheme (DP110100975). R.A.K. acknowledges support from an NSF STC Award (1231306). J.K. acknowledges support by the European Research Council through the Consolidator Grant COMOTION (ERC-614507).